Validation of Supersonic Film Cooling Modeling for Liquid Rocket Nozzle Applications

C. I. Morris[*] and J. H. Ruf[*]

NASA Marshall Space Flight Center, Huntsville, AL, 35812, USA

Supersonic film cooling (SSFC) of nozzles has been used in several liquid rocket engine designs, and is being applied to the nozzle extension of the J-2X upper stage engine now under development. Due to the large size and challenging thermal load of the nozzle extension, there was a critical need to assess the accuracy of CFD models in representative SSFC flowfields. This paper reports results from a CFD analysis of SSFC experiments performed at Calspan in the late 1980s and early 1990s. 2-D and 3-D CFD simulations of flat plate heating, coolant nozzle flow, and film cooling flowfields are discussed and compared with the experimental data. For the film cooling cases studied, the 3-D simulations predict the initial mixing of the coolant and freestream in the adiabatic cooling region reasonably well. However, the CFD simulations generally predict faster mixing in the developed flow region of the flowfield than indicated by the experimental data. Hence, from an engineering perspective, the CFD tool and modeling assumptions used are conservative.

Nomenclature

$\dot{m}$	mass flow rate
$\dot{q}$	heat flux
a	sound speed
d	deflection
I	synthetic schlieren image intensity
k	specific turbulence kinetic energy
M	Mach number, U/a
p	pressure
s	slot height
T	temperature
U	velocity
x	axial distance along test article, $x = 0$ at the coolant injection plane
y	vertical distance from test article, $y = 0$ on the flat plate downstream of the coolant injection plane
y^+	distance from wall in inner-law variables, $\sqrt{\rho_w \tau_w} y / \mu_w$
z	spanwise distance across test article, $z = 0$ on the centerline axis of symmetry of a coolant nozzle

Subscripts

0	stagnation
∞	freestream
aw	adiabatic wall
c	coolant
t	turbulent
w	wall

Symbols

δ_{99}	boundary layer thickness (99% velocity)

---

[*]Aerospace Engineer, Fluid Dynamics Branch/ER42, Senior Member AIAA.

American Institute of Aeronautics and Astronautics

ϵ	specific turbulence dissipation
μ	viscosity
ω	specific turbulence dissipation rate
ρ	density
τ	shear stress
ε	scaling factor in deflection equation

I. Introduction

FILM cooling is used to protect structures in several aerospace applications, such as gas turbine blades, rocket and scramjet combustors, and rocket nozzles. In scramjet combustors and rocket nozzles, the freestream flow, and often the film itself, are supersonic. Supersonic film cooling (SSFC) of nozzles has been used in several liquid rocket engine designs, such as Vulcain, LE-5A, LE-5B and, now under development, the J-2X. The J-2X engine is an upper stage engine with a large area ratio nozzle. The nozzle consists of two sections: a regeneratively cooled section and a radiatively cooled section called the nozzle extension (NE). Between the two sections, the turbine exhaust gas is injected as a film barrier to reduce the heat load to the NE.

SSFC has been studied since the 1960s, with early research being primarily experimental. The pioneering study of Goldstein et al.,[1] at the University of Minnesota, investigated air and helium as coolants with a Mach 3 air freestream. Parthasarathy and Zakkay,[2] at New York University, investigated several coolant gases: air, helium, hydrogen and argon injected into a Mach 6 freestream. Further work at that facility, by Zakkay et al.,[3] investigated the effect of an adverse pressure gradient on SSFC effectiveness.

In the late 1980s and 1990s, several experimental studies were conducted examining SSFC. An investigation of film cooling on a tetracone test article in a Mach 8 freestream was reported by Majeski and Weatherford[4] of McDonnell Douglas. A study using nitrogen and hydrogen coolants in a Mach 3 freestream was conducted by Bass et al.[5] at United Technologies Research Center. Studies using helium coolant in a Mach 6.4 air freestream at Calspan were reported by Holden et al.[6] and Olsen et al.[7] A more detailed report of this effort was provided by Holden and Rodriguez in Ref. 8. A later study using the same Calspan test article and facility, with both hydrogen and helium coolants, was reported by Olsen and Nowak.[9] Air and helium coolants, in a Mach 2.4 freestream, were studied in experimental works by Juhany and Hunt[10] and Juhany et al.[11] at Caltech. The effect of shock impingement on film cooling, of particular importance to the scramjet engine application, was investigated in the Calspan and Caltech efforts. It was also a key focus of the experimental studies, using argon coolant in a Mach 2.35 nitrogen freestream, of Kanda et al.[12] and Kanda and Ono[13] at National Aerospace Laboratory in Japan. A combined experimental and numerical study, using a mixture of cooled nitrogen and air as coolant in a Mach 2.78 air freestream, was conducted by Aupoix et al.[14] at ONERA in France, with a view toward validating analysis tools for nozzle cooling in the Vulcain engine.

Several efforts to numerically model these experiments with CFD have been reported. Chamberlain[15] and Chen et al.[16] simulated the helium coolant Calspan experiments (Refs. 6–8). O'Connor and Haji-Sheikh[17] simulated the earlier work of Ref. 1. Several recent studies have also investigated SSFC from a numerical modeling standpoint. Takita and Musuya[18] numerically investigated shock wave and combustion effects on SSFC using hydrogen. Peng and Jiang[19] have also studied shock waves effects on film cooling, using nitrogen, methane and helium as coolants. Yang et al.[20] have studied both laminar and turbulent film cooling. Recent work by Martelli et al.[21] has numerically investigated SSFC in an advanced dual-bell nozzle design.

The purpose of this paper is to investigate the ability of the Loci-CHEM CFD code[22] to accurately predict SSFC effectiveness in an environment relevant to the J-2X NE. Loci-CHEM is the primary compressible-flow production CFD code in use at NASA Marshall Space Flight Center. CFD analysis was being used extensively during the design cycle of the NE. Due to its large size and challenging thermal load, it was critical to understand the level of accuracy of the CFD simulations of the SSFC fluid dynamics. Recent work by Dellimore et al.[23] has compared the accuracy of subsonic film cooling numerical simulations using Loci-CHEM, and the Spalart-Allmaras turbulence model, with experiments at the University of Maryland. However, early in the NE design cycle it was decided to benchmark Loci-CHEM for SSFC effectiveness in a flow environment similar to that of the J-2X NE. The most representative and best-documented experimental data available were the Calspan film coolant studies (Refs. 6–9).

An overview of the Calspan experiments modeled is given first, followed by a brief summary of Loci-

Table 1. Test conditions for helium film cooling experiments, reproduced from Ref. 8

Run No.	Freestream Conditions				Helium Coolant Conditions			
	p_∞ (psia)	T_∞ (°R)	U_∞ (ft/s)	M_∞	$p_{0,c}$ (psia)	$T_{0,c}$ (°R)	p_c (psia)	$\dot{m}_c$ per nozzle (lbm/s)
4	1.1309	258.44	5063.7	6.423				
43	1.0879	250.66	4994.8	6.433				
44	1.0697	251.81	5003.7	6.430	13.38	530	0.8191	1.629×10^{-3}
45	1.0138	247.52	4962.4	6.432	18.32	530	1.042	2.398×10^{-3}
46	1.0739	252.90	5015.6	6.431	28.12	530	1.498	3.665×10^{-3}
47	1.0573	251.09	4995.7	6.429	38.24	530	1.944	5.071×10^{-3}

CHEM. Comparisons of numerical results with the experimental data are then given for flat plate heating without coolant, the coolant nozzles themselves, and then complete integrated cases with film cooling.

II.   Overview of Calspan Experiments

In this paper, the CFD simulation of the Calspan helium SSFC experiments is described. The hydrogen coolant work in Ref. 9 was modeled as well, and will be reported in a future paper. The Calspan experiments employed a reflected shock tunnel to generate a Mach 6.4 freestream flow around a test article. The freestream gas was air during the helium cooling experiments (Refs. 6–8). Figures 1 and 2, reproduced from Ref. 8, depict the film cooling test article. The approach boundary layer for the freestream flow developed over a flat plate 32.28 inches long. The coolant flow was provided by an array of 40 coolant nozzles, each 0.12 inches high, and 0.404 inches in width at their exit plane. The nozzles used an ideal 2-D contour designed to expand helium to Mach 3. The total step height at the injection plane is 0.14 inches, which includes the 0.12 inch nozzle height and a 0.02 inch lip above the nozzles. Mixing of the film coolant and freestream flows occurred over another 17 inches of flat plate. Note that figure 1 shows the test article set up with a shock generator. The experimental data of interest in this work were the cases without the shock generator. The helium coolant injection was designed to be velocity-matched with the freestream flow.

Flowfield properties for the helium coolant cases modeled in this work are given in table 1. Run number 4 was a flat plate case in which the 17 inch plate downstream of the injection plane was elevated to the same height as the upstream 32.28 inch flat plate. Run number 43 was a case in the nominal film cooling configuration, but without coolant injection. Run numbers 44 through 47 had progressively increasing amounts of helium coolant flow injection.

III.   Modeling Approach

The CFD analysis was performed using the Loci-CHEM CFD code, version 3.2-beta-10 (Ref.22). Loci-CHEM is a finite-volume flow solver for generalized grids developed at Mississippi State University in part through NASA and NSF funded efforts. It uses high resolution approximate Riemann solvers to solve turbulent flows with finite-rate chemistry. Loci-CHEM is comprised entirely of C and C++ code and is supported on all popular UNIX variants and compilers. Efficient parallel operation is facilitated by the Loci[24] framework which exploits multi-threaded and MPI libraries. The code supports the use of a several different RANS turbulence models (Menter's SST and BSL,[25] Wilcox's k-ω,[26] a realizable k-ϵ,[27] and Spalart-Allmaras[28]). Additionally, a hybrid RANS-LES mode is available for the SST, BSL and k-ω models.

In this work, three species were used: helium (for the coolant) and nitrogen and oxygen (as a basic air model). Thermodynamic properties were obtained using a standard partition function formulation which calculates the specific heats, internal energies and entropies of each individual perfect gas species. Laminar
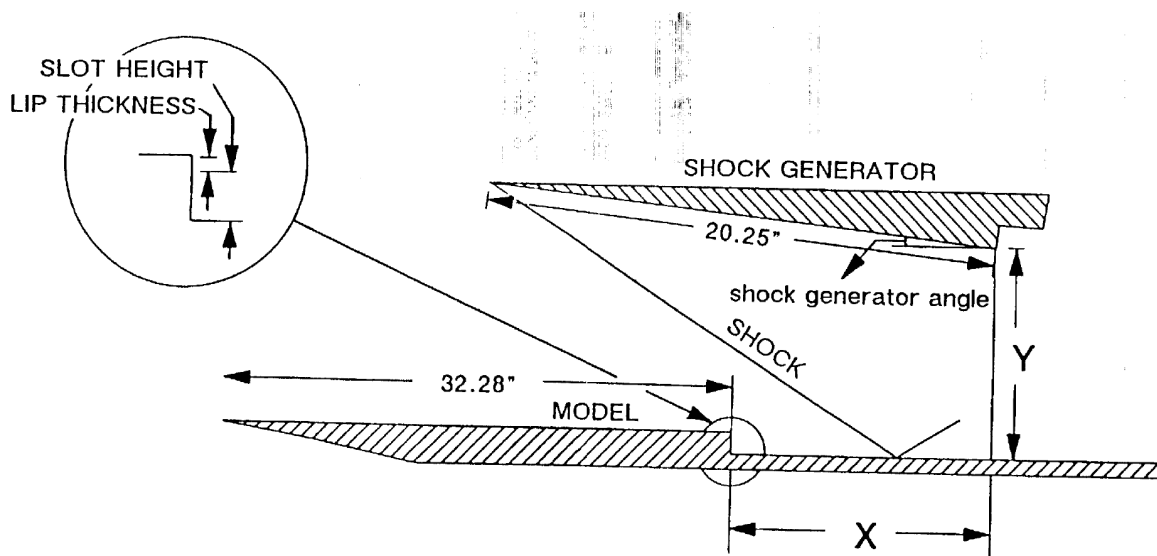
Figure 1. Schematic diagram of test article and shock generator in the Calspan experiments, reproduced from Appendix A of Ref. 8. Note that, in this work, only experiments conducted without the shock generator present were simulated. Dimensions given are in inches.
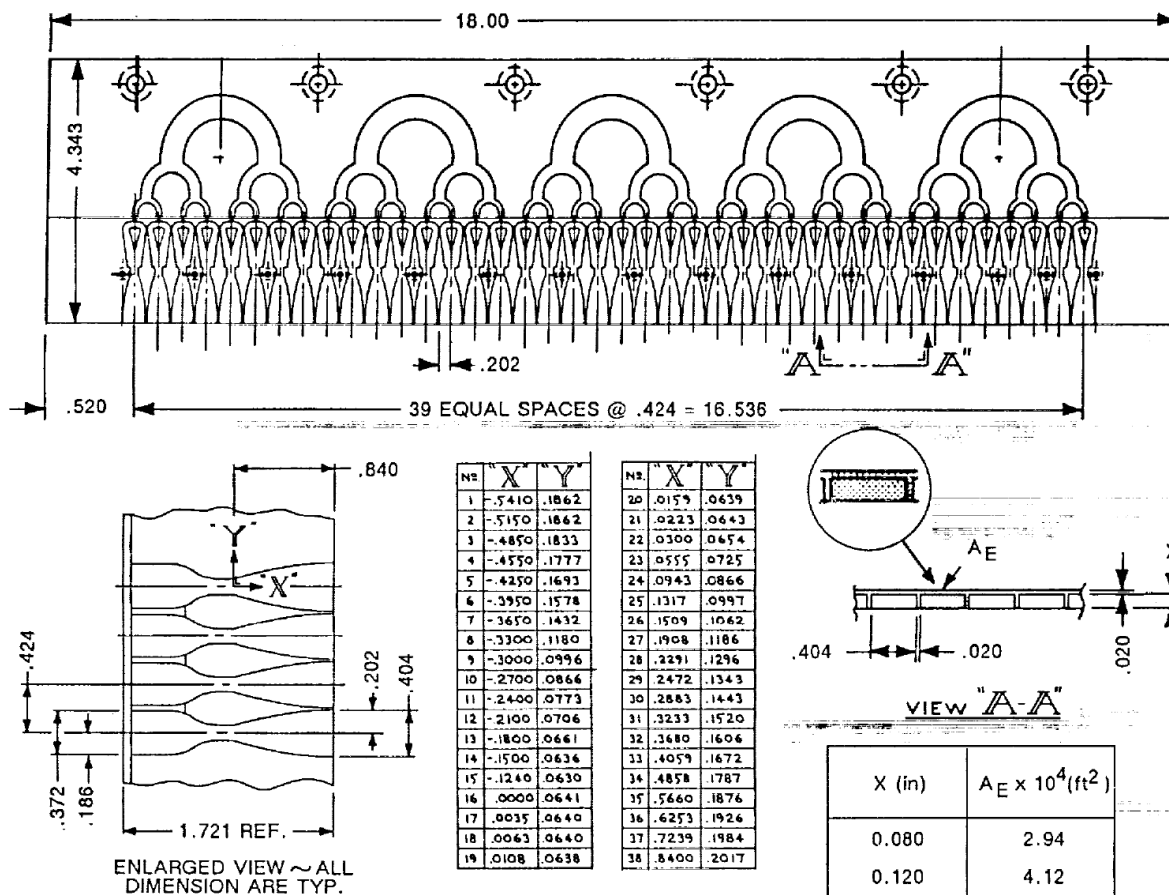

N°	X	Y	N°	X	Y
1	-.5410	.1862	20	.0155	.0639
2	-.5150	.1862	21	.0223	.0643
3	-.4850	.1833	22	.0300	.0654
4	-.4550	.1777	23	.0555	.0725
5	-.4250	.1693	24	.0943	.0866
6	-.3950	.1578	25	.1317	.0997
7	-.3650	.1432	26	.1509	.1062
8	-.3300	.1180	27	.1908	.1186
9	-.3000	.0996	28	.2291	.1296
10	-.2700	.0866	29	.2472	.1343
11	-.2400	.0773	30	.2883	.1443
12	-.2100	.0706	31	.3233	.1520
13	-.1800	.0661	32	.3680	.1606
14	-.1500	.0636	33	.4059	.1672
15	-.1240	.0630	34	.4858	.1787
16	.0000	.0641	35	.5660	.1876
17	.0035	.0640	36	.6253	.1926
18	.0063	.0640	37	.7239	.1984
19	.0108	.0638	38	.8400	.2017

VIEW "A-A"

X (in)	$A_E \times 10^4 (ft^2)$
0.080	2.94
0.120	4.12

ENLARGED VIEW ~ ALL DIMENSION ARE TYP.

Figure 2. Schematic diagram of injector section of the test article in the Calspan experiments, reproduced from figure 13 of Ref. 8. Dimensions given are in inches.

American Institute of Aeronautics and Astronautics

transport property curve fits were obtained using TRANFIT in the CHEMKIN-II software package,[29] and incorporated as inputs into Loci-CHEM. No finite-rate chemistry model was used, and the simulations were run to steady state. Constant turbulent Prandtl and Schmidt numbers of 0.9 and 0.7, respectively, were used in all turbulent CFD simulations. A constant wall temperature, $T_w = 530°$R, was used for the no-slip walls in all simulations.

IV. Results and Discussion

In this study, both 2-D and 3-D simulations were conducted. 2-D simulations of flat plate heating without coolant flow are presented first, with a view toward understanding the basic grid resolution requirements and turbulence model characteristics. The 3-D simulations of the helium coolant nozzles, in which significant 3-D viscous effects developed, are then discussed. Outflow properties from the 3-D nozzle simulations were used to define coolant inflow profiles for 2-D simulations of the film cooling test article flowfield. The 2-D simulations investigated a number of coolant inflow approaches, turbulence models and compressibility corrections. Finally, 3-D simulations of the coupled coolant nozzles and film cooling domain are discussed and compared with the 2-D results.

IV.A. Flat Plate Heating Without Coolant Flow

In this section we examine baseline heating on the test article without film coolant present. All CFD results presented here are obtained with 2-D simulations. The x-y planar grid used for the simulations is shown in figure 3. Loci-CHEM is an unstructured 3-D code, and requires a fully 3-D grid. In the following discussions, 2-D results were obtained by projecting a planar grid one cell in an orthogonal direction. The 2-D grid is a hybrid, unstructured mesh consisting of quadrilaterals near the test model surfaces, and triangles in the far field. The inflow boundaries were set to a supersonic inflow boundary condition, while the outflow boundary was set to a simple extrapolation. A slip wall boundary condition was applied for a short (0.01 inch) length of surface immediately downstream of the left inflow boundary, and upstream of the flat plate leading edge. The remaining surfaces were set to viscous no-slip walls.

The configuration shown in figure 3 applies to run numbers 43 through 47. For the flat plate heating case, run number 4, the backward facing step at the coolant injection plane was eliminated by elevating the plate downstream of the injection plane. The axial grid refinement near the injection plane is eliminated as well.

As is evident in figure 3, the grid spacing is stretched vertically away from the test article surfaces. Near the leading edge of the flat plate, the axial grid spacing is also stretched to better capture the early development of the flat plate boundary layer and the hypersonic viscous interaction in that region. In the baseline grid, the vertical grid spacing was 1.0×10^{-4} inches next to the wall. The vertical spacing grew over 32 cells, and 0.02 inches, to 2.0×10^{-3} inches, and again over 38 cells, and 0.4 inches, to 0.05 inches at the edge of the quadrilateral/triangle transition. There were thus a total of 70 cells in the vertical direction. The axial grid spacing was 1.0×10^{-3} inches at the leading edge of the test article, and stretched over 50 cells, and 1 inch, to a spacing of 0.1 inches. The hyperbolic tangent distribution was used, and the number of grid cells specified was set to limit the stretching rate to ~ 1.1.

The effect of different near-wall vertical spacing, as well as axial spacing, on the computed axial heat flux profile was examined. The SST turbulence model and default Wilcox compressibility correction were used. Calculations with wall vertical spacings of 2.0×10^{-4} and 5.0×10^{-5} inches, with an appropriate decrease or increase in stretched cells, were performed. Typical heat flux values changed by 0.8% when the wall vertical spacing changed from 2.0×10^{-4} to 1.0×10^{-4} inches, and 0.4% going from 1.0×10^{-4} to 5.0×10^{-5} inches. This observation is consistent with the relatively low $y+$ values present: typical values for the baseline grid were ~ 0.3, and were ~ 0.6 and ~ 0.15 for the coarser and finer near-wall spacings, respectively. No effect was seen by varying axial spacing. The axial spacing at the leading edge was held constant, but the largest axial spacing downstream was tested at 0.05 and 0.2 inches.

The effect of turbulence model on the flat plate heating profiles was studied. Results are shown in the left panel of figure 4 for several of the turbulence models available in Loci-CHEM. Calculated profiles for the SST, BSL, and the 1998 and 2008 versions of the Wilcox turbulence models are shown. The k-ϵ and Spalart-Allmaras turbulence models were also tested for this case, but did not result in heat flux profiles sufficiently close to the experimental data to consider using further in this study. The Wilcox compressibility correction,
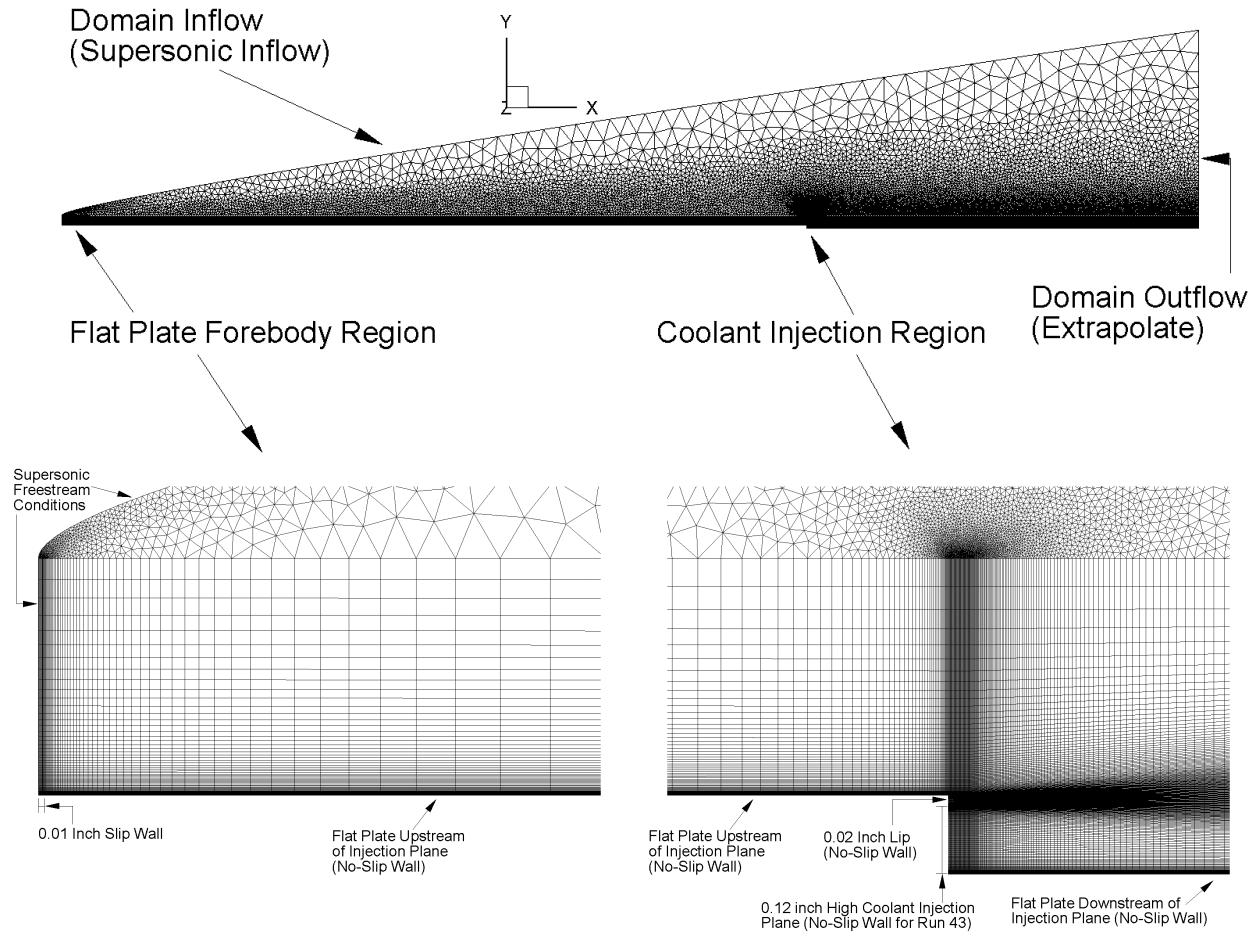
American Institute of Aeronautics and Astronautics

Figure 3. x-y **grid used as the basis for 2-D and 3-D simulations of film cooling on the test article. Closeup views of the flat plate forebody region and the coolant injection region are also shown. For the case of run 4, the 0.14 inch backward facing step is eliminated, and the flat plate downstream of the injection plane is elevated to the level of the upstream flat plate. The additional axial refinement near the injection plane is also eliminated.**

which is the default in Loci-CHEM, was used in all four simulations shown. Also shown is a calculated heat flux profile using the Van Driest-II[30] prediction. For $x > -10$ inches, the Van Driest-II prediction appears to yield the best fit to the experimental data. In comparison, in this region the SST model produces a consistently higher heat flux profile, but appears to be the best of the various CFD models. The BSL and Wilcox 1998 models produce very similar heat flux results, slightly higher than SST, while the Wilcox 2008 model is higher still. The flat plate boundary layer thickness, δ_{99}, at the coolant injection plane ($x = 0$ inch) is 0.33 inches in the SST results, a value which is smaller than the 0.44 inches predicted via analysis and confirmed by flow visualization in Ref. 7.

The effect of compressibility correction on the SST model is shown in the right panel of figure 4. Implementing no compressibility correction results in an axial heat flux profile significantly higher than with the Wilcox or Sarkar corrections, and comparatively poor agreement with the experimental data. This observation is consistent with the results reported by Rumsey.[31] He found that compressibility corrections, while intended for turbulent free-shear flows, and not turbulent boundary layers, do yield improved agreement with the Van Driest-II prediction for highly-cooled walls in hypersonic turbulent boundary layers. In this case, assuming a turbulent Prandtl number of 0.9, $T_{aw} \simeq 1900°$R for $x > -10$ inches, and $T_w/T_{aw} \simeq 0.28$, and as a result, these observations are consistent with those of Ref. 31.

Similar results were obtained in the CFD simulations of the film cooling configuration without film injection (run number 43), shown in figure 5. In the CFD calculation, the coolant inflow boundary was set to a no-slip wall at $T_w = 530°$R. In figure 5, the heat flux profiles are shown on the flat plate downstream of the injection plane. The flow in this region is essentially a thick boundary layer reattaching over a relatively small backward facing step. The CFD simulations predict a rapid rise in heat flux over the first three
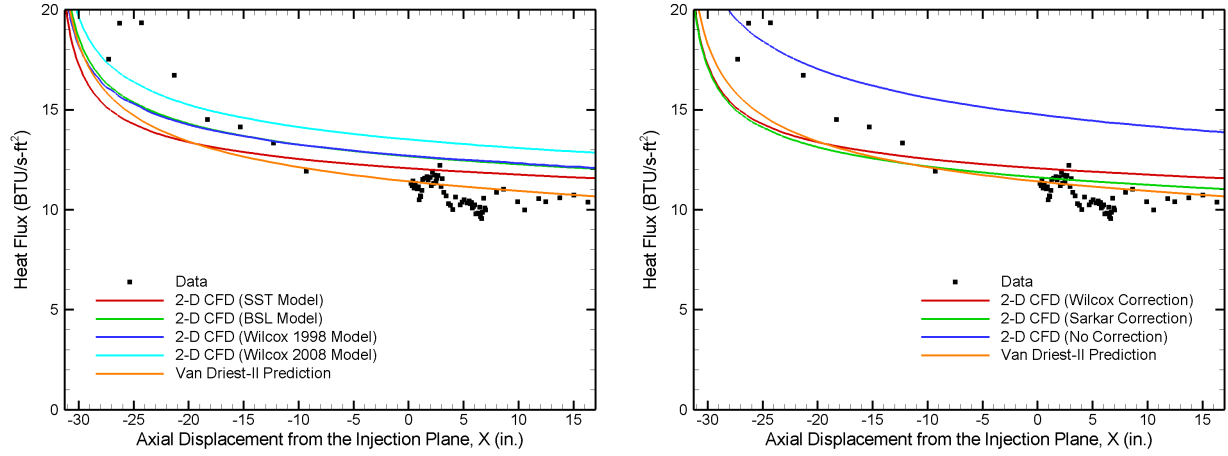
Figure 4. Effect of turbulence model (left panel) and compressibility correction (right panel) on calculated axial heat flux profiles for run number 4. The Wilcox compressibility correction was used for all four turbulence models in the left panel. The turbulence model used in the right panel is SST.
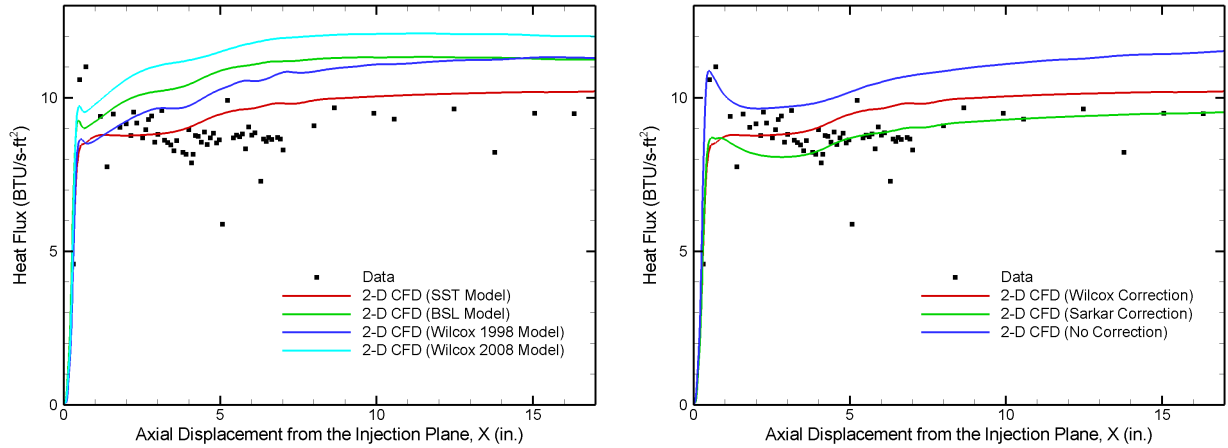

Figure 5. Effect of turbulence model (left panel) and compressibility correction (right panel) on calculated axial heat flux profiles for run number 43. The Wilcox compressibility correction was used for all four turbulence models in the left panel. The turbulence model used in the right panel is SST.

step-heights downstream of the injection plane, and then relaxation to flat plate heating values similar to those of run number 4 (i.e., without a backward facing step). Of the CFD turbulence models tested, SST again agreed best with the experimental data. The BSL, Wilcox 1998 and Wilcox 2008 models yield heat flux results with similar trends to those from run number 4. In the right panel, the Wilcox and Sarkar compressibility corrections again produce better agreement with the experimental data.

IV.B. 3-D Simulations of Helium Coolant Nozzle Flow

The film coolant was injected through an array of nozzles. An isometric sketch of a single coolant nozzle is shown in figure 6. Ref. 7 states that the nozzle contour was designed to ideally expand helium to Mach 3 using a combined method-of-characteristics and viscous analysis strategy. 2-D simulations of the coolant nozzle flow were run in an attempt to duplicate the original design strategy, and 3-D simulations were run to compare with the experimental results. These isolated nozzle simulations were separate from the film cooling domain, and the 3-D solutions were used to obtain inflow boundary conditions for 2-D simulations of the film cooling domain. The 3-D nozzle grid is completely integrated with a 3-D grid of the film cooling domain in subsection IV.D below. The isolated and integrated 3-D coolant nozzle flowfields are very similar, except for minor differences that creep up through the boundary layers near the nozzle exit planes.

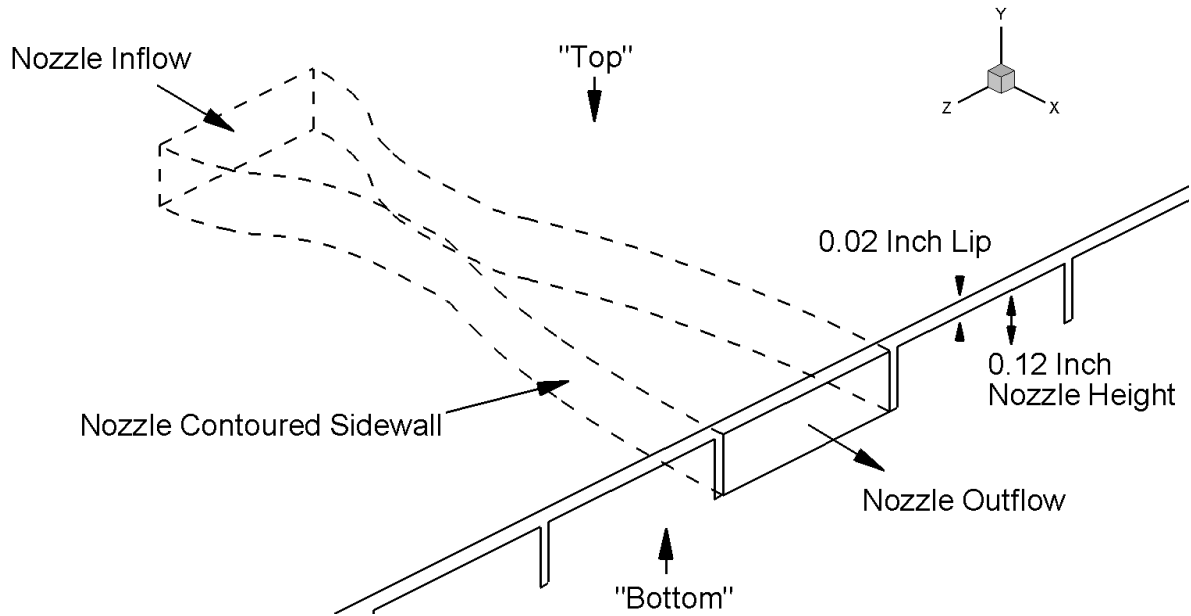The x-z planar half-nozzle grid used as the basis for constructing both the 2-D and 3-D nozzle grids is

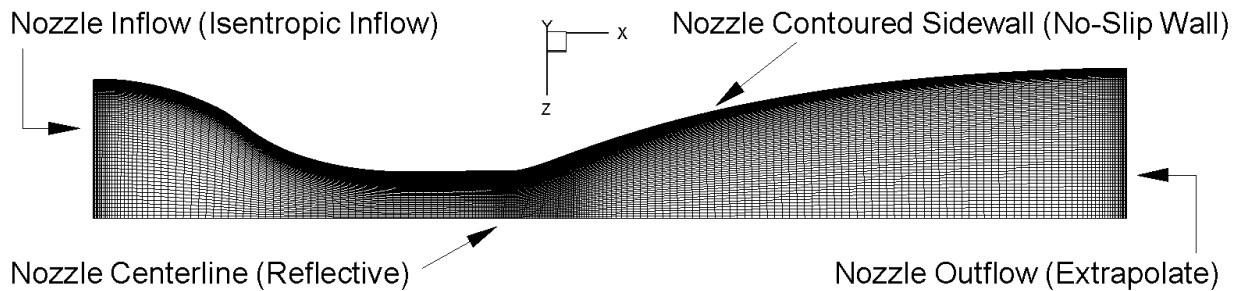**Figure 6. Isometric sketch of a single coolant nozzle**

Figure 7. 229 × 85 cell half-nozzle grid in the x-z plane.

shown in figure 7. The grid was 229 cells in the axial direction, and 85 cells in the transverse direction. The nozzle sidewall contour was generated from the "X" and "Y" coordinates shown in figure 2, with spline interpolation between the points. This contour was set to a no-slip wall. The nozzle inflow boundary was set to an isentropic inflow boundary condition with stagnation pressure and temperature specified. The nozzle outflow exit plane was set to simple extrapolation. The nozzle centerline was set to a reflective plane.

The grid spacing near the nozzle contour was consistent with the values used in the previous subsection: 1.0×10^{-4} inches off the wall, and increasing through a hyperbolic tangent distribution to 2.0×10^{-3} inches over 32 cells, and 0.02 inches. The 2-D grid was constructed by projecting the grid in the x-z plane one cell, for 0.12 inches, in the y-direction. Symmetry boundary conditions were specified on the top and bottom surfaces. The 3-D grid was constructed by projecting the x-z planar grid 90 cells, for 0.12 inches, in the y-direction. No-slip walls were specified for the top and bottom surfaces. The near wall grid spacing on both ends of this projection was consistent with the values described above.

Figure 8 compares the 2-D and 3-D simulations of the nozzle flow. The nozzle stagnation conditions at the inflow plane were set to those for run number 45 of Ref. 8: $p_0 = 18.32$ psia and $T_0 = 530$ °R. In all images shown, the solution was reflected across the nozzle centerline to depict the actual physical situation more clearly. The nozzle top view (a) presents a constant-y plane at $y = 0.06$ inches, halfway up the 0.12 inch height of the nozzle. The nozzle side view (b) presents a constant-z plane at $z = 0$ inches (the nozzle centerline), and the nozzle exit plane view (c) is at $x = 0$ inch, the end the nozzle.

The SST turbulence model with the Wilcox compressibility correction was used for both the 2-D and the 3-D simulations. The default k and ω values for the isentropic inflow boundary condition are 0.001 and 9000,

American Institute of Aeronautics and Astronautics
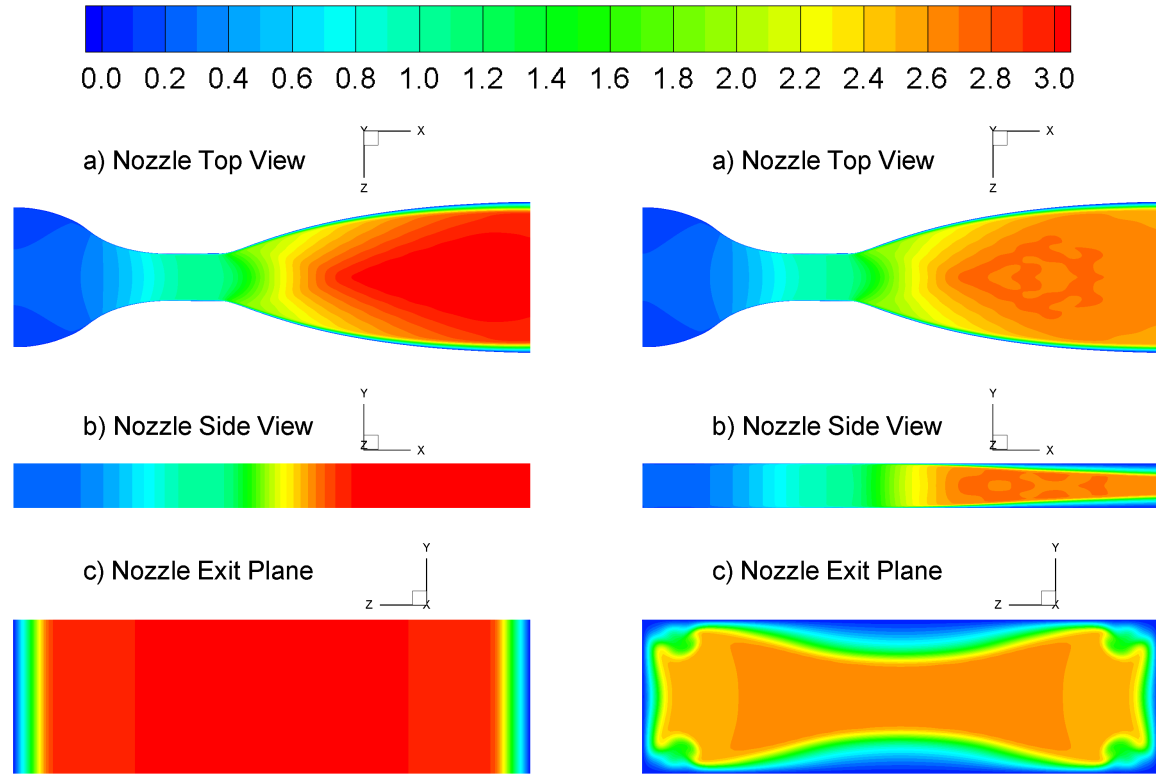
Mach Number

Figure 8. Top, side and exit plane views showing Mach number contours in the helium coolant nozzles. The top view (a) depicts the $y = 0.06$ inch plane, halfway up the nozzle. The side view (b) shows the $z = 0$ inch plane, along the nozzle centerline. The nozzle exit plane view shows the $x = 0$ inch plane; it is not to scale with the top and side views. Left panel: idealized 2-D nozzle flow with slip walls on the top and bottom surfaces. Right panel: actual 3-D nozzle flow with no-slip walls on top and bottom surfaces. Helium inflow conditions are those for run45: $p_0 = 18.32$ psia, $T_0 = 530$ °R. Turbulence Model: SST
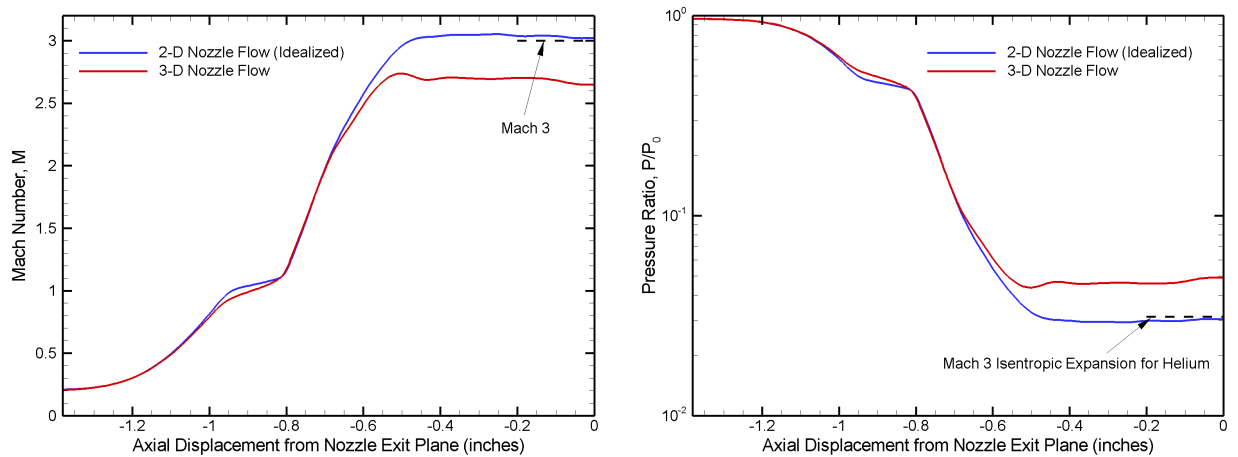
Figure 9. Plots showing nozzle centerline ($z = 0$, $y = 0.06$ inches) flow Mach number (left panel) and pressure ratio (right panel) as a function of axial displacement from the nozzle exit plane. 3-D nozzle flow with no-slip wall boundary conditions on the top and bottom surfaces is compared to idealized 2-D nozzle flow with symmetry boundary conditions on the top and bottom surfaces. Helium inflow conditions are those for run number 45: $p_0 = 18.32$ psia, $T_0 = 530$ °R. Turbulence Model: SST
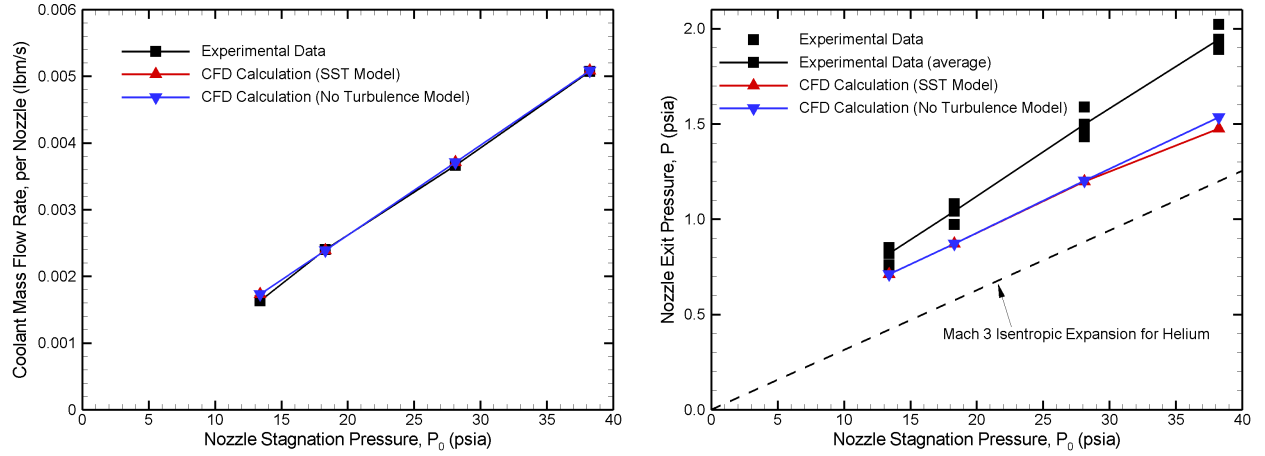
American Institute of Aeronautics and Astronautics

Figure 10. Plots comparing 3-D CFD model results with the experimental data for the helium coolant nozzles. Left panel: coolant nozzle mass flow rate, per nozzle. Right panel: nozzle exit pressure.

respectively, resulting in an inflow turbulence intensity of $\sim 2 \times 10^{-8}$. For this geometry, and these inflow turbulence intensities, none of the turbulence models generated turbulence intensities sufficient to alter the flow from laminar flow for the stagnation conditions of run numbers 44–46. There are some small differences between turbulent and laminar simulations for the conditions of run number 47.

It is evident from the left panel of figure 8 that the 2-D CFD results effectively reproduce the original design strategy for the helium coolant nozzles. The ideal nozzle wall contour produces a relatively uniform Mach 3 core flow free of shock waves. This is also evident from figure 9, in which Mach number (left panel) and pressure ratio, P/P_0, (right panel) are plotted along the nozzle centerline ($z = 0$, $y = 0.06$ inches). The Mach number is slightly higher than Mach 3, and the pressure ratio slightly lower than 0.03125 (the nominal value for an isentropic expansion of helium to Mach 3), for the final half-inch of the nozzle before the exit plane. The nozzle sidewall boundary layer thickness, δ_{99}, at the exit plane is 0.026 inches in the CFD results, a value which is slightly larger than the 0.024 inches predicted in Ref. 7.

In contrast, it is seen in the right panel of figure 8 that, in the 3-D simulation, viscous effects on the top and bottom walls have a significant effect on the core flow. Boundary layer growth constricts the core flow, and prevents expansion of the helium to Mach 3. The effects of weak oblique shocks, emanating from the boundary layers, are evident in the nozzle top and side views. The boundary layer growth is largest along the nozzle centerline. The core Mach number is ~ 2.7 over the final half-inch of the nozzle, with a corresponding pressure ratio of $0.046-0.049$ (figure 9). Similar 3-D effects were also observed in the computational study of Ref. 16.

A comparison of the CFD results of the nozzles with the experimental measurements for run numbers 44–47 is shown in figure 10. Coolant mass flow rate, per nozzle, is shown in the left panel, and nozzle exit pressure is shown in the right panel. The method by which the coolant mass flow rate was experimentally determined is described in detail in Ref. 8. The nozzle exit pressure was measured in the coolant nozzles at an axial location 0.03 inches upstream of the nozzle exit plane. Geometry strongly suggests that the measurement was on the bottom surface of the coolant nozzles, however the exact size and spanwise location of the pressure transducers within the nozzle is uncertain. From examination of the data tables for each run (Appendix A of Ref. 8), it appears that the reported exit pressure was the average of the measured values in five different nozzles.

In figure 10, there is good agreement between the experimental mass flow rate per nozzle and the value calculated from the 3-D CFD results. However, there are significant discrepancies between the experimental nozzle exit pressures and the results from the CFD calculations. The pressure shown in figure 10 for the CFD calculations was extracted along the nozzle centerline, on the bottom ($y = 0$ inch) surface, 0.03 inches upstream from the exit plane. The CFD nozzle exit pressures range from 13% to 24% less than the experimental values. Figure 10 shows, as discussed previously, that the SST model did not generate turbulence intensities sufficient to change the pressure from the corresponding non-turbulent (laminar flow) results with the exception of the highest-pressure condition (run number 47). Note that both the experimental and the CFD results have nozzle exit pressures significantly higher than those predicted for an ideal, isentropic
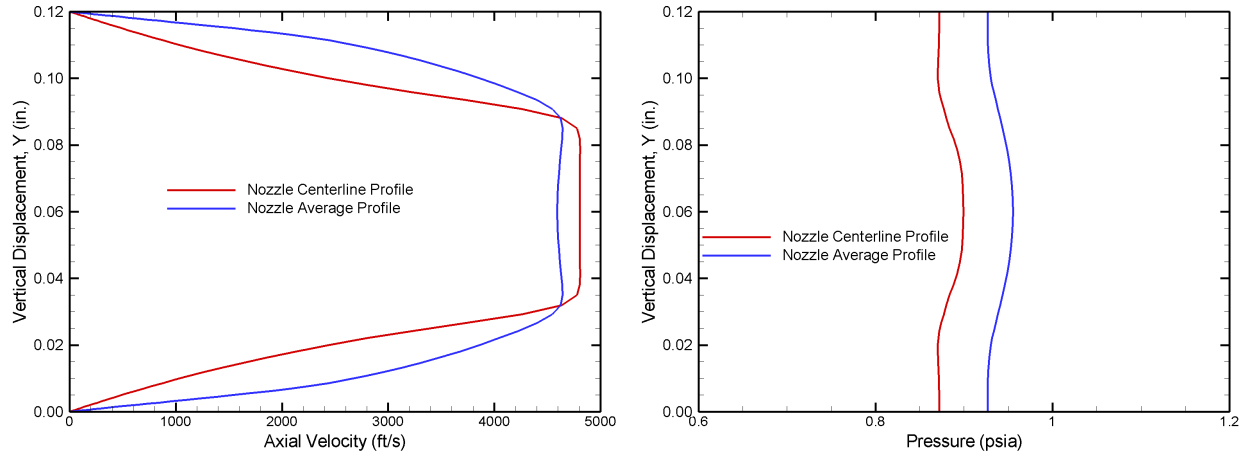
American Institute of Aeronautics and Astronautics

Figure 11. Helium coolant nozzle outflow profiles used as inflow properties for 2-D film-cooling simulations of run number 45. The nozzle exit plane forms a domain in the z-y plane. The nozzle centerline profile was extracted directly from this plane at $z = 0$ inches. The average profile was calculated by integrating each flowfield property in the z-direction, along a constant-y line, and deriving an average value. Turbulence model: SST, with the Wilcox compressibility correction.

expansion of helium to Mach 3.

A number of possibilities have been investigated to explain the disagreement in nozzle exit pressure. Simulations were run with a 3-D grid which had an extra 0.34 inch straight duct upstream of the inflow boundary shown in figure 7, in order to assess the effect of additional boundary layer development upstream of the nozzles. Very little effect on the results was found. Simulations were also run on the original 3-D nozzle grid using inflow k and ω values set to produce an inflow turbulence intensity of 1%, and an inflow viscosity ratio $\mu_t/\mu = 100$. In these cases, the exit pressures decreased slightly, producing comparatively poorer agreement with the experimental data. In these isolated 3-D nozzle simulations, a spanwise average of the pressure at 0.03 inches upstream of the exit can produce better agreement with the data. However, this is not the case for 3-D simulations with the nozzles completely integrated to the film cooling domain. Thus, at this point, the reason for the disagreement remains unexplained.

IV.C.   Two-dimensional Helium Film-Cooling Simulations

In this subsection we discuss a number of parametric studies which were carried out using 2-D simulations of the test article. Although the 2-D approach cannot account for the significant spanwise variation in nozzle outflow properties, it was substantially more economical to conduct parametric studies of turbulence models and compressibility corrections in this manner. These simulations used the 2-D grid shown in figure 3, and used a coolant inflow boundary profile derived from the isolated nozzle simulations discussed in the previous subsection. This approach was previously used by Chen et al.[16] The profiles were extracted from the nozzle exit plane. Effectively, this 2-D approach is an attempt to model the nonuniform coolant nozzle outflow plane as a single linear profile in the y-direction.

Two separate inflow profiles were tried for each case: 1) a centerline profile extracted directly from the nozzle centerline (at $z = 0$ inches), and 2) an average profile obtained by integrating each flowfield property spanwise (in the z-direction) across the nozzle exit plane, for each constant-y line, and deriving an average value. As best as the authors are able to determine from Refs. 6–8, the heat flux gauges in the test article were mounted downstream of the centermost nozzle centerline. Thus, in a certain sense, the centerline profile is the more physically realistic of the two profiles in the near field of the injection plane. However, it also results in an artificially low coolant mass flow rate, in the range of 15–17 % below the nozzle exit plane it was extracted from. Thus, well downstream of the injection region, this profile may have some significant deficiencies. The average profile has a mass flow rate comparatively much closer to the full nozzle, typically in the range of 3–6% less.

Example velocity and pressure profiles corresponding to run number 45 are shown in the left and right panels, respectively, of figure 11. The SST turbulence model with the Wilcox compressibility correction was used for this case. The relatively large boundary layer thickness on the top and bottom of the coolant nozzles

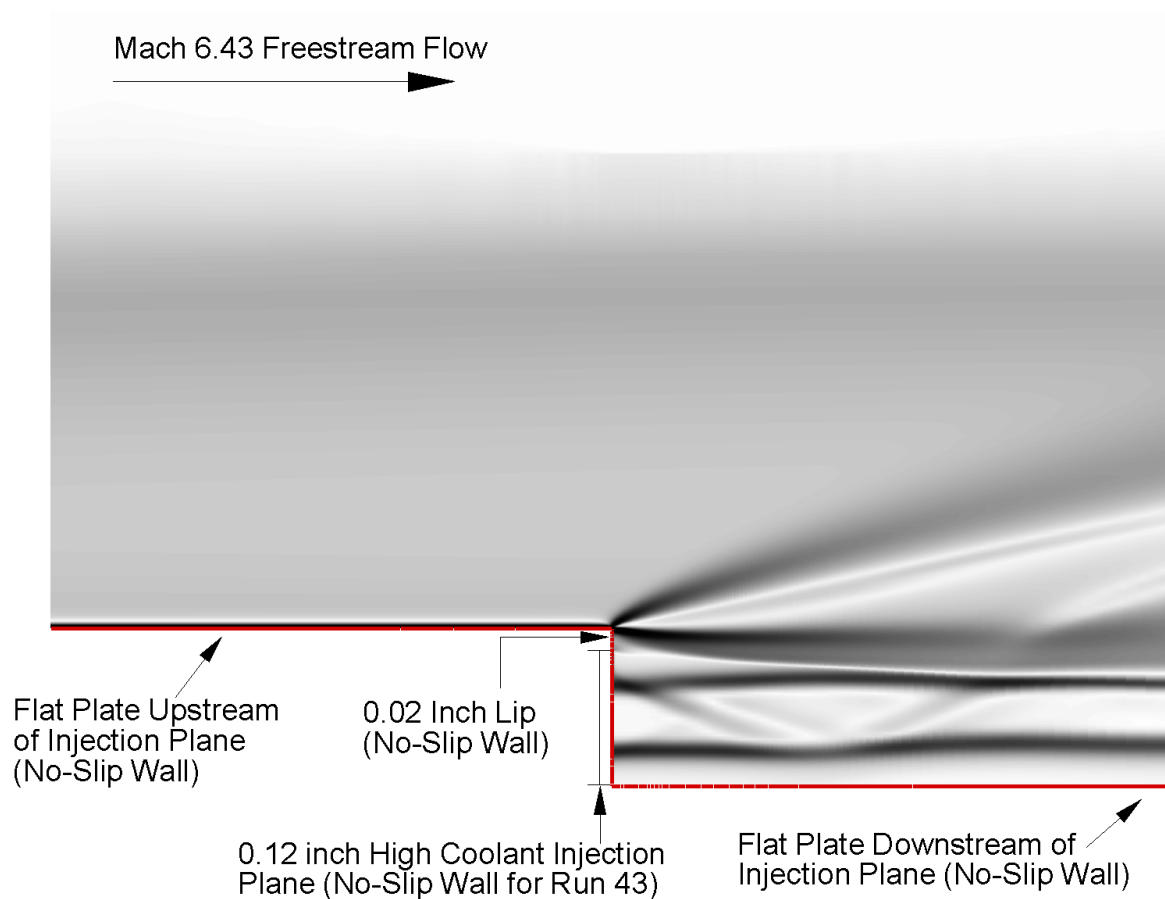American Institute of Aeronautics and Astronautics

Figure 12. Synthetic schlieren image of flowfield in the coolant injection region for run number 45. Inflow profile: coolant nozzle centerline. Turbulence model: SST, with the Wilcox compressibility correction.

is readily apparent from the velocity profiles. The centerline profile has a peak velocity approximately 4% less than a typical $U_\infty \simeq 5000$ ft/s (see table 1) freestream value, while the averaged profile has a peak roughly 8% less. Due to averaging across a wide range of boundary layer thicknesses (see the right panel, part c of figure 8), the average velocity profile has much higher shear near the wall than the centerline velocity profile. The average pressure profile is higher than the centerline profile, and is significantly closer to the average experimental nozzle exit pressure measurement of 1.042 psia. Note as well that the pressure is not constant across either profile. As expected for an isolated nozzle simulation, however, it is symmetric about $y = 0.06$ inches.

The vertical spacing away from the test article wall downstream of the injection plane (see figure 3) is consistent with that used in the flat plate section upstream of the injection plane, as well as in the coolant nozzles: 1.0×10^{-4} inches near the wall, and increasing through a hyperbolic tangent distribution to 2.0×10^{-3} inches over 32 cells, and 0.02 inches. Consistent with the nozzle grid, 90 cells are used across the 0.12 inch coolant inflow plane. Another 40 cells are used across the 0.02 inch lip, with spacing of 1.0×10^{-4} inches on both ends of the lip. Thus, including the 70 vertical cells from the upstream quadrilateral portion of the grid, the total number of vertical cells in the quadrilateral portion of the grid downstream of the injection plane is 200. The axial spacing was set to 1.0×10^{-3} inches for 0.04 inches downstream of the injection plane, and then stretched over 100 cells, and 0.96 inches, to a final uniform axial spacing of 0.05 inches for the remaining 16 inches of the domain. The effect of axial grid spacing on heat flux profiles was tested by evaluating final uniform wall spacings of 0.025 and 0.1 inches. No difference in axial heating profile was found.

A "synthetic schlieren" image of the injection near field of run number 45 is shown in figure 12. The image is intended to highlight the density gradients in the flowfield, and was obtained using the SST model,
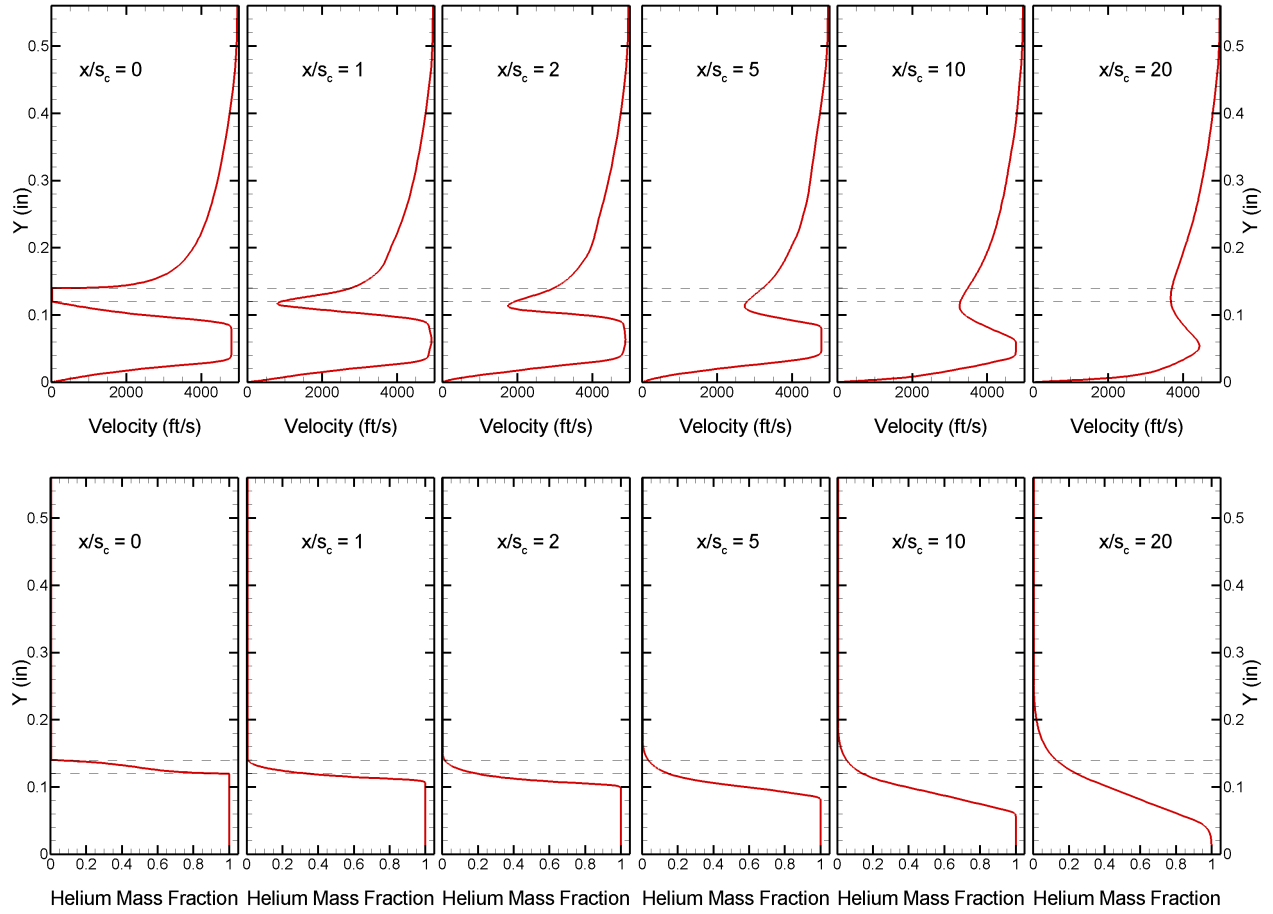
American Institute of Aeronautics and Astronautics

Figure 13. Axial velocity (upper panel) and helium mass fraction (lower panel) profiles at various axial stations downstream of the coolant injection plane for run number 45. The dashed lines show the height of the coolant slot, and the slot plus the lip. Inflow profile: coolant nozzle centerline. Turbulence model: SST, with the Wilcox compressibility correction.

with the Wilcox compressibility correction, and using the centerline coolant inflow profile. The greyscale image is proportional to I^2, where

$$I = \begin{cases} 1 - d & \text{if } d < 1 \\ 0 & \text{if } d \geq 1 \end{cases} \tag{1}$$

and the deflection d is given by

$$d = \varepsilon \sqrt{\left(\frac{\partial \rho}{\partial x}\right)^2 + \left(\frac{\partial \rho}{\partial y}\right)^2} \tag{2}$$

where $\varepsilon = 0.01$ was used for the images in this paper. This formula is an approximation to a bright-field light source and spatial filter pair.[32]

It is evident from figure 12 that the boundary layer approaching the coolant injection plane is relatively large compared to the coolant injection height. As the boundary layer is highly cooled, there are large density gradients across it which make it visible in the image. The same is true of the coolant boundary layer downstream of the injection plane. The freestream flow expands over the backward facing step at the injection plane through a Prandtl-Meyer expansion wave. Pressure equilibration between the freestream flow and the coolant inflow then produces a series of oblique shock waves within the coolant stream.

Axial velocity and helium mass fraction profiles for run number 45, using the centerline coolant inflow profile, are shown at several different axial stations in figure 13. The axial distance from the injection plane, x, is normalized by the coolant slot height, s_c. Normalized axial stations, x/s_c, of 0, 1, 2, 5, 10, and 20 are shown. Dashed lines depict the height of the coolant slot, and the slot plus the lip. The velocity profile

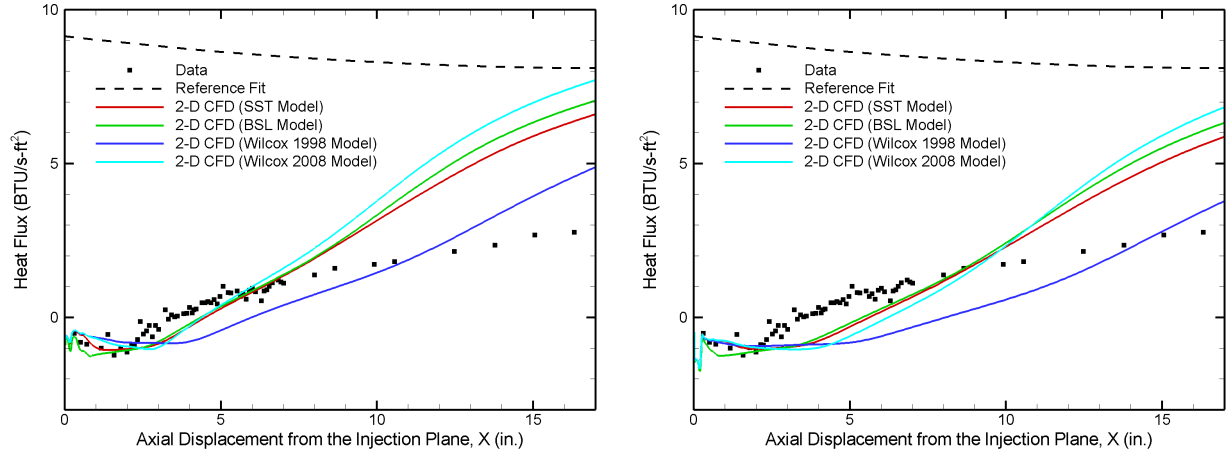American Institute of Aeronautics and Astronautics

Figure 14. Effect of turbulence model on 2-D calculated axial heat flux profiles for run number 45. The Wilcox compressibility correction, which is the default one in Loci-CHEM, was used for all four turbulence models. Left panel: coolant nozzle centerline inflow profile. Right panel: coolant nozzle average inflow profile.
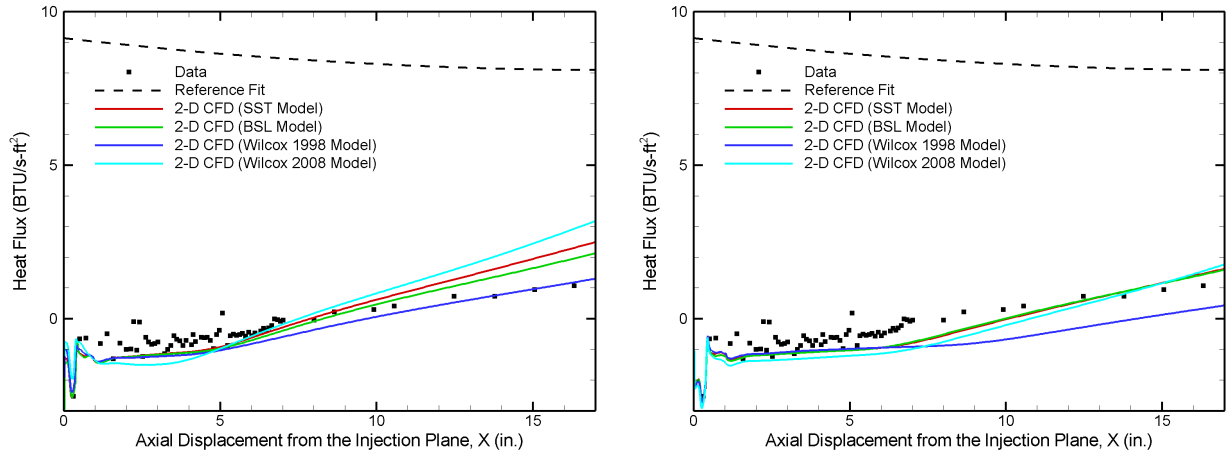

Figure 15. Effect of turbulence model on 2-D calculated axial heat flux profiles for run number 47. The Wilcox compressibility correction, which is the default one in Loci-CHEM, was used for all four turbulence models. Left panel: coolant nozzle centerline inflow profile. Right panel: coolant nozzle average inflow profile.

at the injection plane ($x/s_c = 0$) is as expected: the centerline coolant velocity profile from the left panel of figure 11 may be seen in the lower part of the profile from $y = 0$ to 0.12 inches. The velocity is zero along the lip wall surface, and then rapidly increases toward the freestream value through a comparatively large turbulent boundary layer profile. The incoming boundary layer thickness in the coolant stream is approximately twice the lip width, while the freestream turbulent boundary layer thickness is over 16 times larger than the lip. At one slot height downstream ($x/s_c = 1$), the velocity profile is similar to that at the injection plane, but a wake-like mixing of the two streams is evident. Due to the size of the boundary layers in the two streams, this wake-like mixing initially occurs at velocities much lower than the $U_\infty \simeq 5000$ ft/s freestream and coolant core velocities. At $x/s_c = 1$ the velocity defect (with respect to the freestream) is quite large, 84%. It is 65% at $x/s_c = 2$, 45% at $x/s_c = 5$, and 35% at $x/s_c = 10$. At $x/s_c = 20$, the defect is still evident, though at this point the coolant stream core velocity has decreased to roughly 4500 ft/s, and the coolant boundary layer on the lower wall has fully transitioned to a turbulent profile. By this point, it may be seen from the lower panel that the freestream gas has penetrated about two-thirds of the way across the coolant flow. Thus, in contrast to a classic mixing layer velocity profile, the near-field turbulent mixing between the coolant and freestream here is dominated by a wake-like mixing process. The same phenomena is seen in the 2-D results for the other film cooling cases.

The effect of coolant inflow profile and turbulence model on the axial film cooling heating profiles was studied. Results are shown in figures 14 (run number 45) and 15 (run number 47) for the SST, BSL, and the

American Institute of Aeronautics and Astronautics

1998 and 2008 versions of the Wilcox turbulence models. The default Wilcox compressibility correction was used for all turbulence models. It should be noted that for each run number and turbulence model studied, a separate nozzle case was run using that turbulence model. Results using the centerline coolant inflow profile are presented in the left panels of figures 14 and 15, while results using the average coolant inflow profile are depicted in the right panels. Also shown in the figures is a reference flat plate heating profile used in Ref. 7. The equation is

$$\dot{q}(x) = 9.14 - 0.119x + 0.0034x^2 \tag{3}$$

where $\dot{q}$ is in BTU/ft^2-s and x is in inches. As it is based on a nominal freestream condition, this relation does not exactly represent the flat plate heating for a specific run. However, it does provide a representative reference point in the figures.

It may be seen from figures 14 and 15 that, in both the CFD simulations and the experimental data, there is initially a length of minimal heat flux in which the coolant at the wall is uncontaminated by the freestream gas (i.e., the adiabatic cooling length). Note that neither coolant inflow profile in the CFD results for run number 45 exactly predicts the adiabatic cooling length in the experimental data, while the CFD results for run number 47 predict this length more accurately. For both runs, the centerline coolant profile does a better job at predicting this length than the average coolant profile. However, the centerline inflow profile also has a comparatively worse agreement with the slope of the data in the developed flow region (the downstream region in which the freestream gas has mixed to the wall and is increasing the heat flux). This is likely due to the lower coolant mass flow rate of this profile. Overall, neither coolant inflow profile, with any of the turbulence models, produced good agreement with the experimental data in the developed flow region for run number 45, while, again the agreement for run number 47 is considerably better. It appears that the experimental data for run number 45 exhibit, at the end of the adiabatic cooling length, a sharp rise in heat flux, followed by a gradual relaxation of the slope. The CFD calculations fail to predict the decreased slope in the experimental heat flux profile after the initial rise. The reason for the poor agreement for run number 45 is currently unknown.

The SST, BSL and 2008 Wilcox models produce similar heat flux profiles. All three have nearly identical adiabatic cooling lengths, with relatively minor differences in the slope of the heat flux profile in the developed flow region. For both runs, the 1998 Wilcox model consistently produces a longer adiabatic cooling length than the other three models, and a more gradual slope for the heat flux profile in the developed flow region.

The effect of turbulence model compressibility correction on the film cooling heat flux profiles was also investigated. Results are shown in figure 16 for run number 45, and figure 17 for run number 47. All simulations were run with the SST turbulence model. Again, for each run number and compressibility implementation, a separate nozzle case was run. As was seen in the earlier flat plate heating results, implementing either the Wilcox or Sarkar corrections results in a lower heat flux profile than the use of no correction. The Sarkar correction yields the lowest slope of the heat flux profile in the developed region, and has the best agreement with the experimental data. The two coolant inflow profiles exhibit the same trends here as was the case in the turbulence model comparisons above.

IV.D. Three-dimensional Helium Film-Cooling Simulations

It is evident from the previous section that the flow nonuniformities present in the coolant outflow make accurate 2-D simulations of the Calspan experiments a challenging task. After gaining insight and experience with the 2-D simulations, we conducted 3-D simulations of the film-cooling experiments. The 3-D grid was generated from the 2-D x-y grid shown in figure 3. Spanwise, the computational domain comprises half of a single coolant nozzle (0.202 inches at the nozzle exit, and see figure 7), plus half of the wall width between the coolant nozzles (0.01 inches), for a total spanwise width of 0.212 inches. By setting reflective boundary conditions on both sides of the spanwise direction, effectively an infinite array of cooling nozzles is simulated. In this approach, flowfield symmetry across the nozzle centerline, and from nozzle to nozzle, is assumed. 100 cells total were used in the spanwise direction, with 85 dedicated to the half-nozzle, and 15 to half of the inter-nozzle wall. Clustering was used in the vicinity of the nozzle sidewall (see figure 7). This clustering was relaxed away from the coolant nozzles: for $x > 1$ inch, the spanwise spacing was uniform at 2.12×10^{-3} inches. The resulting 3-D grid comprised ~ 16.5 million cells.

The previous sections have shown that the SST turbulence model with a compressibility correction performed reasonably well at predicting flat plate heat flux distribution. Although none of the turbulence models did a consistently good job of predicting the film cooling data in the 2-D film cooling simulations,
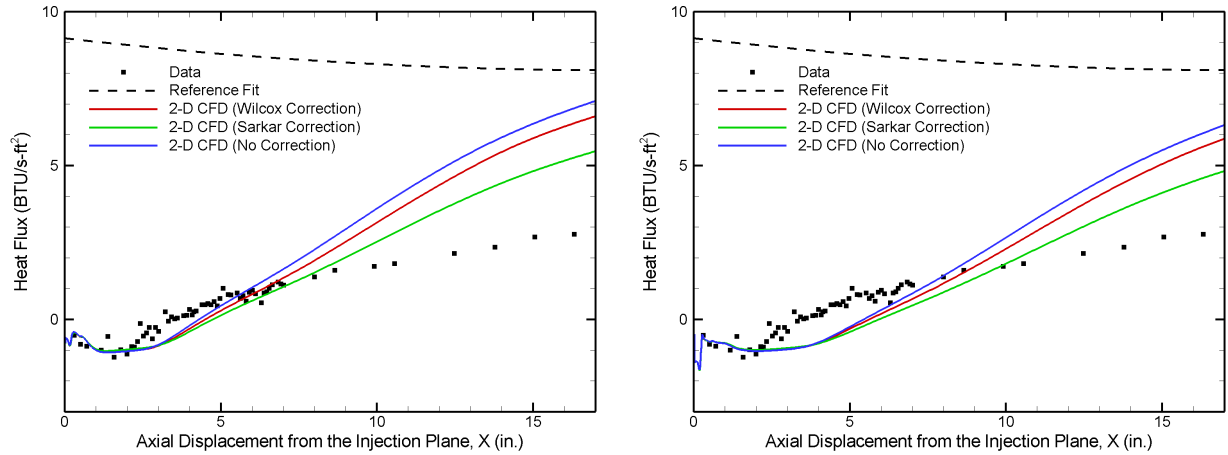
Figure 16. Effect of compressibility correction on 2-D calculated axial heat flux profiles for run number 45. The SST turbulence model was used for all cases. Left panel: coolant nozzle centerline inflow profile. Right panel: coolant nozzle average inflow profile.
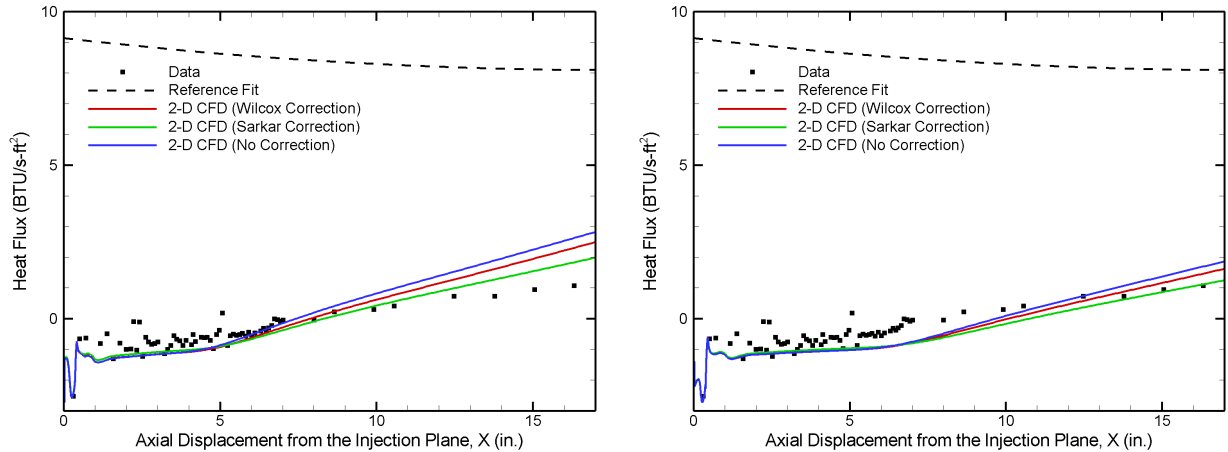

Figure 17. Effect of compressibility correction on 2-D calculated axial heat flux profiles for run number 47. The SST turbulence model was used for all cases. Left panel: coolant nozzle centerline inflow profile. Right panel: coolant nozzle average inflow profile.

SST performed no worse than the other models. Therefore, in the 3-D simulations, only SST was employed, with both the Wilcox and Sarkar compressibility corrections implemented.

Top and isometric views of the heat flux distribution on the flat plate and coolant nozzle bottom surfaces are shown for run number 45 in figure 18. For illustration, the computed flowfield has been reflected and copied to represent three nozzle widths. The top view shows these surfaces in their true proportion, while in the isometric view the spanwise dimension (z) has been scaled by a factor of ten. The results shown used the Wilcox compressibility correction. As expected from the previous section, the heat flux generally increases downstream of the injection plane. However, it is apparent from the figure that there is considerable spanwise variation in the heat flux distribution across each coolant nozzle. The heat flux is at a peak along the centerline of a nozzle, and generally at a minimum downstream of the wall between the nozzles.

The 3-D heat flux results along the nozzle centerline are compared with the film cooling experimental data for run numbers 44–47 in figures 19–22. Also shown in the figures are the 2-D heat flux profiles from the previous section using the coolant nozzle centerline inflow profile. As stated previously, as best as the authors are able to determine from Refs. 6–8, the heat flux gauges in the test article were mounted downstream of the centermost nozzle centerline. However, the explicit spanwise width of the gauges is not provided in the references, adding some uncertainty to our comparisons with the data. On the assumption that the heat flux gauge widths in figure 14 of Ref. 8 are to scale, a width of 0.2 inches can be estimated. Therefore, also shown in figures 19–22 are centerline average heat flux profiles, which are a spanwise average heat flux over

American Institute of Aeronautics and Astronautics

Heat Flux Contours in Top View (Correct Scale)
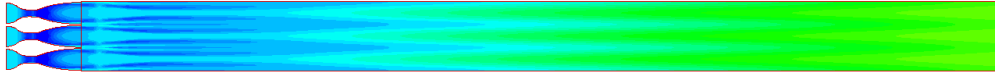
Heat Flux Contours in Isometric View (Z Axis Scaled by 10)
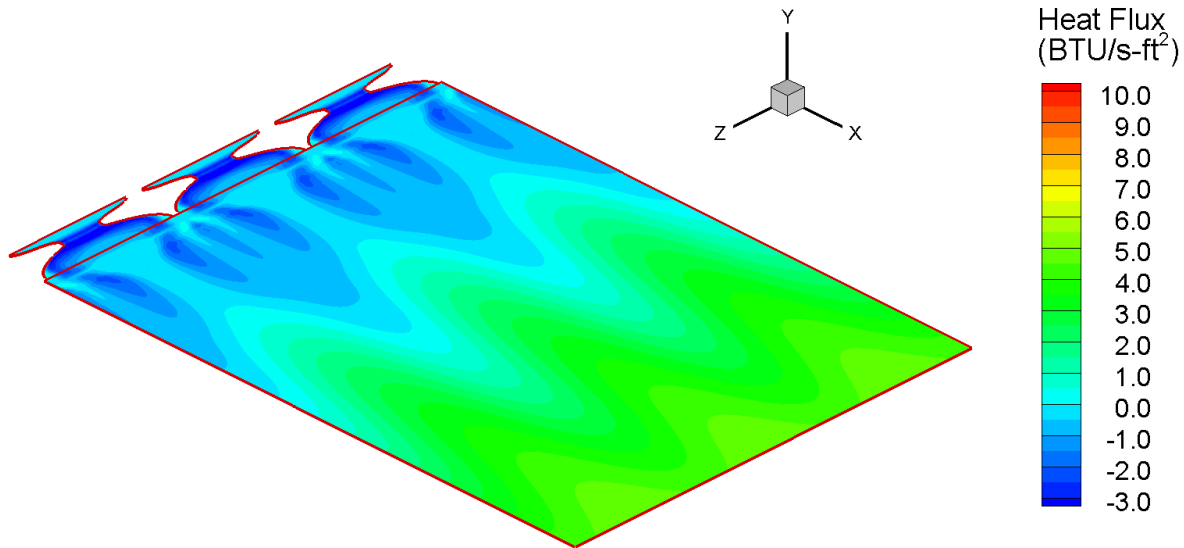

Figure 18. Surface heat flux contour plots showing axial and spanwise variation in heat flux from 3-D simulation of run number 45. For illustration, the computed flowfield has been reflected and copied to represent three nozzle widths. Turbulence model: SST, with the Wilcox compressibility correction.

a 0.2 inch width about the nozzle centerline ($z = -0.1$ to $+0.1$ inches).

In comparing the 3-D CFD results with the experimental data, we again make the distinction between the adiabatic cooling and the developed flow regions. It is evident that CFD results modestly overpredict the adiabatic cooling length for run numbers 44 and 45, while for run numbers 46 and 47 the agreement is good. In the developed flow region, the agreement between the 3-D CFD results and the data remains generally poor for run numbers 44–46. It should be noted, however, that near the end of the film cooling domain, the slope of the 3-D heat flux profiles has better agreement with the data than the 2-D profiles. This is likely due to the correct overall coolant mass flow rate in the 3-D simulations. The agreement in the developed flow region for run number 47 is reasonably good, though this region is naturally the shortest here of all the runs investigated. In summary, it appears that the 3-D CFD results do a relatively good job of predicting the near field mixing in the adiabatic cooling region, and in contrast, a too-rapid mixing of the coolant and and freestream flows in the developed flow region.

Note that the largest differences between the 3-D centerline and centerline average heat flux profiles are in the adiabatic cooling region, and the early developed flow region. As is evident from figure 18, this is due to the greater spanwise variation in heat flux closer to the injection plane.

The Sarkar compressibility correction results in a consistently lower heat flux profile in the developed flow region than the Wilcox correction. The Sarkar results are in better agreement with the data, consistent with the flat plate heating results discussed previously.

A curious feature of the 2-D and 3-D heat flux profiles is the differences in heat flux level in the adiabatic cooling region. The 2-D results have a typical adiabatic cooling region heat flux of -1.0 to -1.2 BTU/s-ft^2, while the 3-D centerline results are in the range of -0.3 to -0.5 BTU/s-ft^2. The centerline average profiles
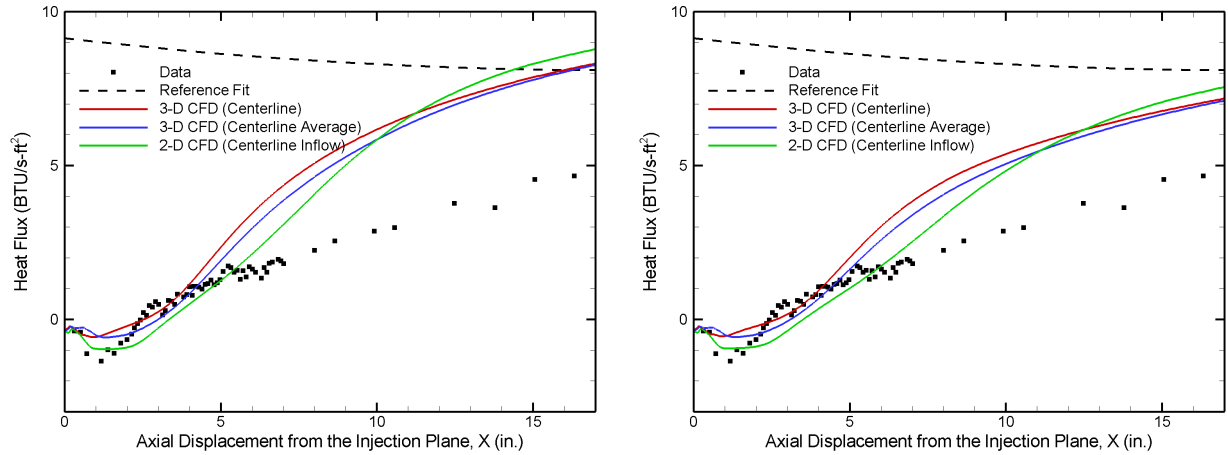
Figure 19. Effect of compressibility correction on 2-D and 3-D calculated centerline axial heat flux profiles for run number 44. Left panel: Wilcox correction. Right panel: Sarkar correction. The SST turbulence model was used for all cases. The centerline average profile is a 0.2 inch spanwise average about the nozzle centerline. The 2-D CFD results used the coolant nozzle centerline inflow profile.
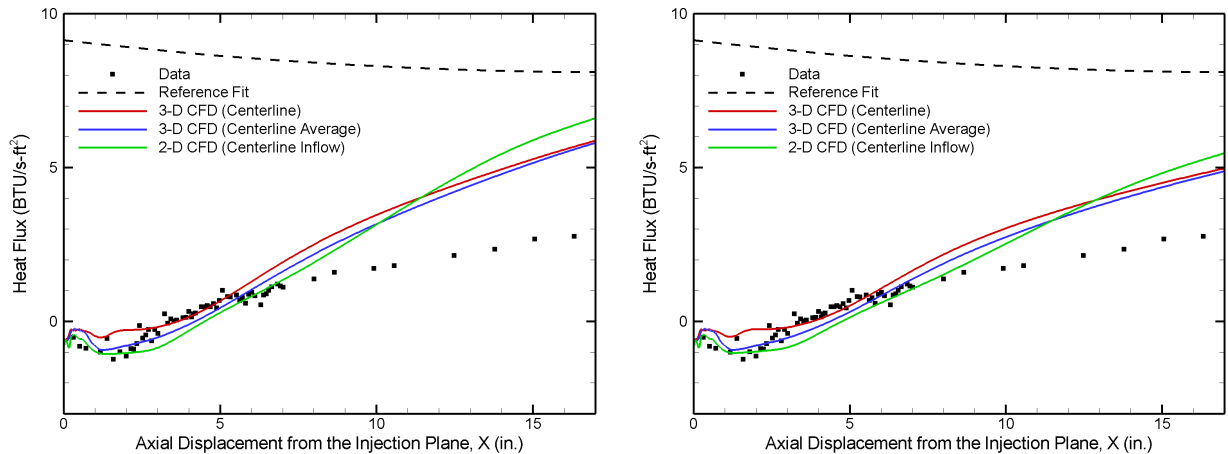

Figure 20. Effect of compressibility correction on 2-D and 3-D calculated centerline axial heat flux profiles for run number 45. Left panel: Wilcox correction. Right panel: Sarkar correction. The SST turbulence model was used for all cases. The centerline average profile is a 0.2 inch spanwise average about the nozzle centerline. The 2-D CFD results used the coolant nozzle centerline inflow profile.

are intermediate between the two. The heat fluxes are negative because the adiabatic wall temperature of the helium coolant is less than the wall temperature. The differences exist in all four of the runs studied. As the 2-D CFD results used the coolant centerline inflow profile, and the 3-D results were extracted directly along the nozzle centerline, the question naturally arises as to why there are differences in heat flux the adiabatic cooling region. Inspection of the solution flowfields reveals that the boundary layer directly along the nozzle centerline grows more rapidly downstream of the injection plane in the 3-D simulations than in the 2-D simulations, resulting in a smaller absolute heat flux. This is due to 3-D adaptation of the nonuniform coolant boundary layer in the 3-D simulations to expansion waves in both the x-y and x-z planes.

Axial velocity and helium mass fraction profiles confirm that the initial wake-like mixing of the coolant and freestream flows that was present in the 2-D simulations is also the 3-D simulations. Along the nozzle centerline, the breakdown of the coolant core is accelerated by the more rapid growth of the coolant boundary layer at that location.
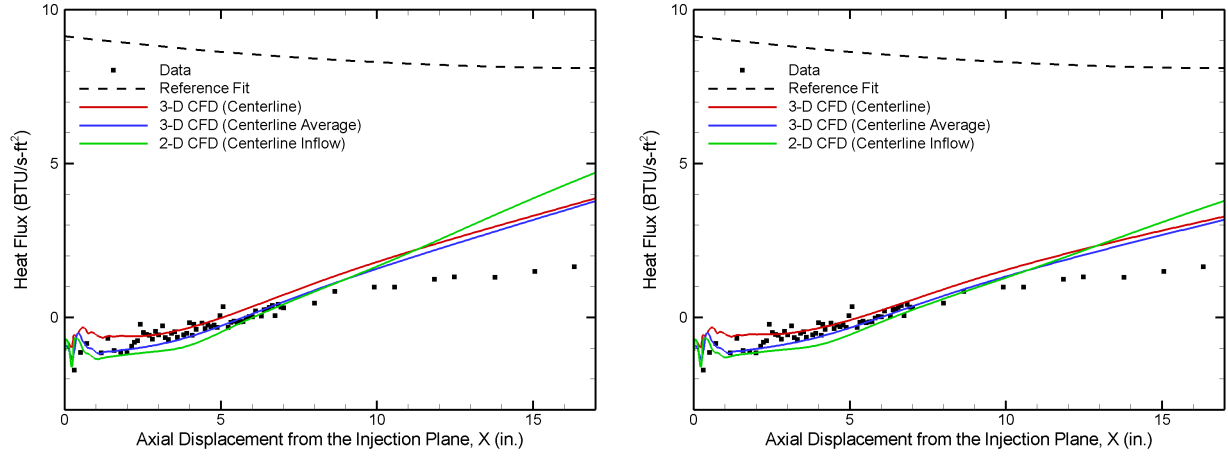
American Institute of Aeronautics and Astronautics

Figure 21. Effect of compressibility correction on 2-D and 3-D calculated centerline axial heat flux profiles for run number 46. Left panel: Wilcox correction. Right panel: Sarkar correction. The SST turbulence model was used for all cases. The centerline average profile is a 0.2 inch spanwise average about the nozzle centerline. The 2-D CFD results used the coolant nozzle centerline inflow profile.

Figure 22. Effect of compressibility correction on 2-D and 3-D calculated centerline axial heat flux profiles for run number 47. Left panel: Wilcox correction. Right panel: Sarkar correction. The SST turbulence model was used for all cases. The centerline average profile is a 0.2 inch spanwise average about the nozzle centerline. The 2-D CFD results used the coolant nozzle centerline inflow profile.
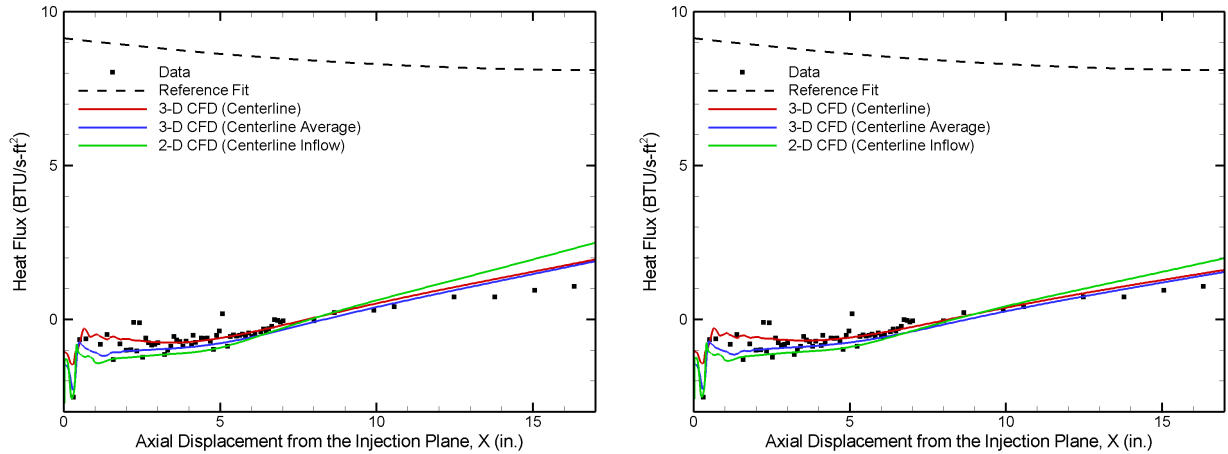
V. Summary

In an effort to benchmark Loci-CHEM for SSFC flowfields for the J-2X program, SSFC experiments conducted at Calspan in the late 1980s and early 1990s were simulated and analyzed. These experiments were selected for study because they were well-documented, readily available, and physically relevant to SSFC on the J-2X NE. However, in the course of this investigation, some key knowledge gaps about the experiments arose: specifically, the precise size and spanwise location of the coolant nozzle exit pressure transducers, and the spanwise width of the heat flux gauges.

This study investigated the experiments in a building-block approach, first simulating the flat plate heating results without film cooling present on a 2-D grid. The hypersonic turbulent boundary layers present in the experiments were highly cooled, and compressibility corrections were found to improve agreement between the CFD heat flux results and the experimental data.

Next, a single coolant nozzle was simulated on a 3-D grid, with a view toward gaining insight in that flowfield, as well as providing a nozzle exit plane from which physically relevant profiles could be extracted as inflow boundary conditions for 2-D film cooling simulations. 3-D viscous effects were observed in the coolant nozzles, leading to significant flow nonuniformities at the nozzle exit plane. The experimental coolant mass flow rates were well-predicted by the CFD simulations. However, there were unresolved discrepancies between

American Institute of Aeronautics and Astronautics

the CFD results and nozzle exit pressure data.

The effect of several CFD modeling parameters were then investigated using 2-D simulations of the film cooling domain. Given the coolant nozzle flow nonuniformities, reducing the nozzle exit plane to a single linear profile for an inflow boundary is a crude approximation. However, two different coolant inflow profile approaches were investigated: a coolant nozzle centerline profile, and a coolant nozzle average profile. The centerline profile produced a better prediction of the adiabatic cooling length than the average profile, but a poorer prediction of the slope of the heat flux profile in the developed region of the flowfield. The SST, BSL and 2008 Wilcox turbulence models performed similarly, and compressibility corrections again improved agreement with the experimental data.

After gaining insight and experience with the 2-D simulations, we conducted 3-D simulations of the film-cooling experiments. Significant spanwise variation in the film cooling heat flux distribution was noted in the 3-D results. The lack of precise heat flux gauge width information adds uncertainty to comparisons of of the CFD results with the experimental data. However, the 3-D results generally provide a reasonable prediction of the adiabatic cooling length. Agreement with the slope of the experimental heat flux data in the developed flow region is less good. However, the 3-D simulations do give a better prediction of the experimental slope here than in comparable 2-D simulations. This is likely due to better modeling of the coolant mass flow rate in the 3-D approach. From an engineering perspective, in these 3-D simulations Loci-CHEM and the modeling assumptions employed were conservative.

A key feature observed in both the 2-D and 3-D film cooling simulations was the initial wake-like mixing between the freestream and coolant streams. The core of the coolant flowstream is nearly velocity matched with the freestream. However, the freestream boundary layer is large compared to the height of the coolant stream, so that the coolant flow is initially mixing with a much slower freestream gas. The wake-like velocity profile persists through at least 20 coolant slot heights downstream.

Acknowledgments

References

[1]Goldstein, R. J., Eckert, E. R. G., Tsou, F. K., and Haji-Sheikh, A., "Film Cooling with Air and Helium Injection through a Rearward-Facing Slot into a Supersonic Air Flow," *AIAA Journal*, Vol. 4, No. 6, 1966, pp. 981–985.

[2]Parthasarathy, K. and Zakkay, V., "An experimental Investigation of Turbulent Slot Cooling at Mach 6," *AIAA Journal*, Vol. 8, No. 7, 1970, pp. 1302–1307.

[3]Zakkay, V., Wang, C. R., and Miyazawa, M., "Effect of Adverse Pressure Gradient on Film Cooling Effectiveness," *AIAA Journal*, Vol. 12, No. 5, 1974, pp. 708–709.

[4]Majeski, J. A. and Weatherford, R. H., "Development of an Empirical Correlation for Film-Cooling Effectiveness," AIAA Paper 88-2624, June 1988.

[5]Bass, R., Hardin, L., Rodgers, R., and Ernst, R., "Supersonic Film Cooling," AIAA Paper 90-5239, Oct. 1990.

[6]Holden, M. S., Nowak, R. J., Olsen, G. C., and Rodriguez, K. M., "Experimental Studies of Shock Wave/Wall Jet Interaction in Hypersonic Flow," AIAA Paper 90-0607, Jan. 1990.

[7]Olsen, G. C., Nowak, R. J., Holden, M. S., and Baker, N. R., "Experimental Results for Film Cooling in 2-D Supersonic Flow Including Coolant Delivery Pressure, Geometry, and Incident Shock Effects," AIAA Paper 90-0605, Jan. 1990.

[8]Holden, M. S. and Rodriguez, K. M., "Experimental Studies of Shock Wave/Wall Jet Interaction in Hypersonic Flow," NASA CR 195197, May 1994. See also NASA CR 195844, May 1994.

[9]Olsen, G. C. and Nowak, R. J., "Hydrogen Film Cooling With Incident and Swept-Shock Interactions in a Mach 6.4 Nitrogen Free Stream," NASA TM 4603, June 1995.

[10]Juhany, K. A., Hunt, M. L., and Sivo, J. M., "Influence of Injectant Mach Number and Temperature on Supersonic Film Cooling," *Journal of Thermophysics and Heat Transfer*, Vol. 8, No. 1, 1994, pp. 59–67.

[11]Juhany, K. A. and Hunt, M. L., "Flowfield Measurements in Supersonic Film Cooling Including the Effect of Shock-Wave Interaction," *AIAA Journal*, Vol. 32, No. 3, 1994, pp. 578–585.

[12]Kanda, T., Ono, F., and Saito, T., "Experimental Studies of Supersonic Film Cooling with Shock Wave Interaction," AIAA Paper 96-2663, July 1996.

[13]Kanda, T. and Ono, F., "Experimental Studies of Supersonic Film Cooling with Shock Wave Interaction (II)," *Journal of Thermophysics and Heat Transfer*, Vol. 11, No. 4, 1997, pp. 590–593.

[14]Aupoix, B., Mignosi, A., Viala, S., Bouvier, F., and Gaillard, R., "Experimental and Numerical Study of Supersonic Film Cooling," *AIAA Journal*, Vol. 36, No. 6, 1998, pp. 915–923.

[15]Chamberlain, R., "Computation of Film Cooling Characteristics in Hypersonic Flow," AIAA Paper 92-0657, Jan. 1992.

[16]Chen, Y. S., Chen, C. P., and Wei, H., "Numerical Analysis of Hypersonic Turbulent Film Cooling Flows," AIAA Paper 92-2767, May 1992.

[17]O'Connor, J. P. and Haji-Sheikh, A., "Numerical Study of Film Cooling in Supersonic Flow," *AIAA Journal*, Vol. 30, No. 10, 1992, pp. 2426–2433.

[18]Takita, K. and Masuya, G., "Effects of Combustion and Shock Impingement on Supersonic Film Cooling by Hydrogen," *AIAA Journal*, Vol. 38, No. 10, 2000, pp. 1899–1906.

[19]Peng, W. and Jiang, P.-X., "Influence of Shock Waves on Supersonic Film Cooling," *Journal of Spacecraft and Rockets*, Vol. 46, No. 1, 2009, pp. 67–73.

[20]Yang, X., Badcock, K. J., Richards, B. E., and Narakos, G. N., "Numerical Simulation of Film Cooling in Hypersonic Flows," AIAA Paper 2003-3631, June 2003.

[21]Martelli, E., Nasuti, F., and Onofri, M., "Numerical Analysis of Film Cooling in Advanced Rocket Nozzles," *AIAA Journal*, Vol. 47, No. 11, 2009, pp. 2558–2566.

[22]Luke, E. A., Tong, X., Wu, J., Tang, L., and Cinnella, P., "A Step Towards 'Shape-Shifting' Algorithms: Reacting Flow Simulations Using Generalized Grids," AIAA Paper 2001-0897, Jan. 2001.

[23]Dellimore, K. H., Marshall, A. W., Trouve, A., and Cadou, C. P., "Numerical Simulation of Subsonic Slot-Jet Film Cooling of an Adiabatic Wall," AIAA Paper 2009-1577, Jan. 2009.

[24]Luke, E. A., *A Rule-Based Specification System for Computational Fluid Dynamics*, Ph.D. thesis, Mississippi State University, Mississippi, 1999.

[25]Menter, F. R., "Two-Equation Eddy-Viscosity Turbulence Models for Engineering Applications," *AIAA Journal*, Vol. 32, No. 8, 1994, pp. 1598–1605.

[26]Wilcox, D. C., *Turbulence Modeling for CFD*, DCW Industries, Inc., 2006, pp. 124–128.

[27]Shih, T.-H., Liou, W. W., Shabbir, A., Yang, Z., and Zhu, J., "A New k-ϵ Eddy Viscosity Model for High Reynolds Number Turbulent Flows," *Computers & Fluids*, Vol. 24, No. 3, 1995, pp. 227–238.

[28]Spalart, P. R. and Allmaras, S. R., "A One-Equation Turbulence Model for Aerodynamic Flows," AIAA Paper 92-0439, Jan. 1992.

[29]Kee, R. J., Dixon-Lewis, G., Warnatz, J., Coltrin, M. E., and Miller, J. A., "A Fortran Computer Code Package for the Evaluation of Gas-Phase Multicomponent Transport Properties," Sandia National Laboratories Report SAND86-8246, December 1986.

[30]Van Driest, E. R., "The Problem of Aerodynamic Heating," *Aeronautical Engineering Review*, Vol. 15, No. 10, 1956, pp. 26–41.

[31]Rumsey, C. L., "Compressibility Considerations for $k-\omega$ Turbulence Models in Hypersonic Boundary-Layer Applications," *Journal of Spacecraft and Rockets*, Vol. 47, No. 1, 2010, pp. 11–20.

[32]Settles, G. S., *Schlieren and Shadowgraph Techniques: Visualizing Phenomena in Transparent Media*, Springer, 2001, pp. 116–118.